Dynamical thermal conductivity of suspended graphene ribbons in the hydrodynamic regime

Arnab K. Majee and Zlatan Aksamija

Phys. Rev. B **98**, 024303 — Published 5 July 2018

DOI: 10.1103/PhysRevB.98.024303

Dynamical Thermal Conductivity of Suspended Graphene Ribbons in the Hydrodynamic Regime

Arnab K. Majee and Zlatan Aksamija*

Department of Electrical and Computer Engineering

University of Massachusetts Amherst, Amherst, MA 01003-9292, USA

Abstract

The steady-state behavior of thermal transport in bulk and nanostructured semiconductors has been widely studied, both theoretically and experimentally. On the other hand, fast transients and frequency dynamics of thermal conduction has been given less attention. The frequency response of thermal conductivity has become more crucial in recent years, especially in light of the constant rise in the clock frequencies in microprocessors and terahertz sensing applications. Thermal conductivity in response to a time-varying temperature field starts decaying when the frequency exceeds a cut-off frequency Ω_c, which is related to the inverse of phonon relaxation time τ, on the order of 2-10 ps in most bulk semiconductors. Phonons in graphene have much longer phonon relaxation times, which we show leads to far lower Ω_c. Our calculations, based on the phonon Boltzmann equation coupled with first-principles dispersion, show that dynamical thermal conductivity of graphene resembles a low-pass filter that decays beyond an Ω_c ranging from 100 MHz to 10 GHz, controlled by temperature and ribbon width. The response parallels the Drude model of electrons, but with far lower cut-off. Moreover, the presence of strong normal processes in graphene results in a complex-valued conductivity and gradual transition around Ω_c, with the resistive contribution to the heat flux having higher cutoff frequency and smaller phase lag than the hydrodynamic part. The dynamical conductivity will impact dissipation in high-frequency applications of graphene. Our findings also provide a platform for future studies of hydrodynamic transport and wave-like, or *second sound*, heat transfer by tuning the frequency of the applied temperature field.

I. INTRODUCTION

In the context of developing of on-chip heat management, thermoelectric, and other energy conversion applications, the ability to tailor the thermal conductivity of a material is of fundamental importance. The steady-state behavior of the thermal transport in bulk semiconductors,[1,2] metals[3] and, more recently, in two-dimensional (2D) materials[4–8] has been widely studied, expanding the upper[9] and lower[10] bounds on thermal conductivity. Significant efforts have also been devoted to understand the reduction of thermal conductivity due to atomically rough interfaces[11–13] and boundaries[14–16] in nanostructured materials ranging from nanowires[17–19] to thin films,[20,21] superlattices,[22–25] and nanocomposites.[26,27] Heat conduction at short length scales, comparable to the phonon mean-free-path (MFP), and from small heat sources is a related type of size effect that has also drawn significant research attention in recent years.[28–30] When the temperature gradient varies over a length scale comparable to the phonon MFP, Fourier's concept of local thermal equilibrium breaks down[31,32] and transport becomes nonlocal[33] and partially ballistic.[34,35]

To treat this situation, Mahan[36] proposed a nonlocal theory of heat conduction, while Chen[37] derived ballistic-diffusive heat equations to capture this nondiffusive nature of phonons. There have been numerous observations of the reduced thermal transport at length scales comparable to the phonon MFP[38–41] and the interplay between phonon MFP spectra and size effects is now quite well understood.[42,43] On the other hand, the effect of fast transients and the frequency response of thermal conduction, sometimes called the *dynamical* thermal conductivity, has been given less attention. The response of thermal conductivity to rapidly varying heat sources may become more crucial in the future, especially with the constant growth in the clock frequencies in microprocessors and increase in giga- and terahertz applications of semiconductor devices. Analogous to transport at short scales in nanostructures, transport of heat at short time scale smaller than the phonon lifetime also becomes non-diffusive in nature, where local non-equilibrium prevails. It has been theoretically predicted in 3D materials that the heat flux in response to a time-varying temperature gradient starts decaying when the frequency of the applied heat source (Ω) exceeds a certain cut-off frequency Ω_c, which was related to the inverse of the average phonon relaxation time τ_C.[44–46] This dynamical and transient behavior has also been quantified in metals[47–49] and argon crystals.[50]

Using molecular dynamics simulation, Volz[44] found that the phonon relaxation time in bulk semiconductors such as silicon is short, on the order of 30-140 ps, and concluded that a frequency-

dependent behavior of thermal conductivity can only be observed when the applied temperature gradient is varying at frequencies exceeding 10 gigahertz (GHz). Sellitto and co-workers[51] used a phonon-hydrodynamical model with suitable boundary conditions to study the frequency dependent thermal conductivity in silicon nanowires, while Yang and Dames[52] extended the gray BTE model for periodic heating on the surface of bulk materials. Ezzahri and Joulain[46] solved the Boltzmann-Peierls transport equation in the frequency domain within single-mode relaxation time (SMRT) approximation and used the Debye-Callaway model[53] to obtain expressions for dynamical thermal conductivity of natural silicon and germanium crystals, and semiconductor alloys $Si_{0.7}Ge_{0.3}$, $In_{0.53}Ga_{0.47}As$, and $In_{0.49}Ga_{0.51}P$. Among these materials, $Si_{0.7}Ge_{0.3}$ alloys exhibited the most pronounced dynamical thermal conductivity trend with cut-off frequencies ranging from 0.1 megahertz (MHz) at 3 K to 2 GHz at the room temperature. Chaput[54] solved frequency-dependent phonon Boltzmann transport equation (pBTE) by linearizing it and transforming it into an integral equation over the irreducible Brillouin zone to compute dynamical thermal conductivity in diamond, silicon, and magnesium silicide. The frequency-dependent behavior was observed only beyond 10 GHz, corroborating the results of Volz.[44]

In contrast to the aforementioned bulk semiconductors, 2D materials, especially graphene, have longer phonon relaxation times.[55] The presence of strong momentum-conserving normal phonon-phonon processes in graphene, overshadowing momentum-destroying umklapp processes, results in hydrodynamic transport.[56,57] Therefore, in suspended graphene and wide graphene ribbons the cut-off frequency Ω_c is much lower than that of silicon, even at room temperature. This could impact thermal dynamics and transients[58] in graphene at comparatively lower frequency ranges. Therefore, the dynamical thermal conductivity is expected to play a significant role in removing heat from electronic devices based on graphene and other related two-dimensional materials switching at high frequencies. Some of the other interesting phenomena that can be studied using dynamical thermal conductivity are Poiseuille flow[59] and *second sound*, where heat does not diffuse but rather propagates in a wave-like fashion.[60–63] This phenomenon, which has been observed at low temperatures in liquid helium,[64] NaF,[65,66] Bi,[67,68] and $SrTiO_3$,[69] was predicted from first-principles calculations to persist even at room temperature in graphene.[56]

II. METHODOLOGY

In this paper, we focus on the dynamical thermal conductivity of suspended graphene ribbons. We calculate a frequency-dependent thermal conductivity by solving the time-dependent phonon Boltzmann transport equation (pBTE). In response to a rapidly time-varying temperature field, the heat conduction in solids becomes non-local in time and space $\kappa(\vec{r},t;\vec{r'},t')$.[70] Phonons that are driven by a temperature gradient at position $\vec{r'}$ and time t', move from $\vec{r'}$ to $\vec{r}$ in time between t' and t to cause a heat current at position $\vec{r}$ and time t. The heat current $J(\vec{r},t)$ is given by the convolution of thermal conductivity with the temperature gradient $\nabla_{\vec{r}}T$ at position $\vec{r'}$ and time t' as[42]

$$J(\vec{r},t) = -\int d\vec{r'}dt'\kappa(\vec{r},t;\vec{r'},t')\nabla_{\vec{r}}T(\vec{r'},t').$$

It is mathematically convenient to express the heat current in Fourier domain, where the convolution becomes a simple product of a frequency- and wavenumber-dependent thermal conductivity and temperature gradient. On taking the Fourier transform of the time-domain heat current, we get

$$\widetilde{J}(\vec{Q},\Omega) = -\widetilde{\kappa}(\vec{Q},\Omega)\times\widetilde{\nabla}T(\vec{Q},\Omega), \tag{1}$$

where $\widetilde{J}(\vec{Q},\Omega)$, $\widetilde{\kappa}(\vec{Q},\Omega)$ and $\widetilde{\nabla}T(\vec{Q},\Omega)$ are the Fourier-transformed heat current, thermal conductivity, and temperature gradient, respectively, while Q and Ω are the wavenumber and frequency of the temperature gradient.

The time-dependent pBTE is given by

$$\frac{\partial N_{q,b}(\vec{r},t)}{\partial t} + \vec{v}_{q,b}\cdot\nabla_{\vec{r}}N_{q,b}(\vec{r},t) = \left[\frac{\partial N_{q,b}(\vec{r},t)}{\partial t}\right]_{coll}, \tag{2}$$

where $N_{q,b}(\vec{r},t)$ is the phonon distribution function, which is a function of position $\vec{r}$ as well as time t. From here on, we suppress $(\vec{r},t)$ in $T(\vec{r},t)$ and $N_{q,b}(\vec{r},t)$, and $(\vec{Q},\Omega)$ in $\widetilde{N}_{q,b}(\vec{Q},\Omega)$ for clarity, where $\widetilde{N}_{q,b}(\vec{Q},\Omega)$ is the Fourier-transformed distribution function. $\vec{v}_{q,b} = \partial\omega_{q,b}/\partial q$ is the group velocity of the phonon wavevector q in branch b, $\omega_{q,b}$ being its vibrational frequency. Using Callaway's idea,[53] we write the collision term as the sum of two terms

$$\left[\frac{\partial N_{q,b}}{\partial t}\right]_{coll} = -\left(\frac{N_{q,b}-N^0_{q,b}}{\tau^R_{q,b}}\right) - \left(\frac{N_{q,b}-N^*_{q,b}}{\tau^N_{q,b}}\right), \tag{3}$$

where the first term on the right hand side of the equation represents the rate at which the non-equilibrium distribution returns to the equilibrium Bose-Einstein distribution $N^0_{q,b} = [\exp(\hbar\omega_{q,b}/k_BT)-1]^{-1}$ due to momentum-destroying resistive scattering mechanisms. The second term represents

how the perturbed distribution function in the presence of collective momentum-conserving normal phonon-phonon processes relaxes to a drifted distribution $N^*_{q,b}$, often referred to as *flowing equilibrium*. The flowing equilibrium distribution is written as $N^*_{q,b} = [\exp(\hbar\omega_{q,b}/k_BT + \vec{\lambda}\cdot q) - 1]^{-1}$, where $\vec{\lambda}$ is the displacement vector of the drifted distribution and is related to the drift velocity by $\vec{\lambda} = \hbar\vec{\nu}_d/k_BT$. The $\tau^R_{q,b}$ and $\tau^N_{q,b}$ are the average resistive and normal scattering times respectively.

Resistive processes include umklapp phonon-phonon processes, isotope, and line-edge roughness scattering so the resistive scattering rate is calculated by combining them as $1/\tau^R_{q,b} = 1/\tau^U_{q,b} + 1\Big/\tau^{Iso}_{\omega_q} + 1/\tau^{LER}_{q,b}$. While Callaway's approach of separating the collision integral into resistive and normal components is not as exact as the iterative[71–73] and direct pBTE solvers,[74] it has been widely used and shown to be reasonably accurate in graphene[75] and graphite ribbons[76] when combined with *ab initio* dispersion. Here we compute the phonon dispersion of suspended graphene from first-principles Density Functional Theory (DFT) as implemented in the open-source package *Quantum Espresso*.[77] The expressions for all the relevant scattering rates, including anharmonic umklapp and normal phonon-phonon,[78] isotope,[79] and line-edge roughness,[80] are taken from our recent work[8] and given for reference in the Supplemental Material.[81]

The deviation of the phonon distribution function from equilibrium is $\Phi_{q,b}(\vec{r},t) = N_{q,b} - N^0_{q,b}$. We detail the derivation of this deviated distribution in frequency domain $\widetilde{\Phi}_{q,b}(Q,\Omega)$ in the Appendix; once it is obtained, the non-local heat current is related to $\widetilde{\Phi}_{q,b}(Q,\Omega)$ through

$$\widetilde{J}(Q,\Omega) = -\widetilde{\kappa}(Q,\Omega)\times\widetilde{\nabla}T(Q,\Omega) = \sum_{q,b}\hbar\omega_{q,b}v_{q,b}\widetilde{\Phi}_{q,b}(Q,\Omega) \tag{4}$$

from which we obtain an expression for the frequency-dependent thermal conductivity composed of two parts $\kappa_{eff}(Q,\Omega) = \kappa_{RTA}(Q,\Omega) + \kappa_{corr}(Q,\Omega)$. The $\kappa_{RTA}(Q,\Omega)$ is the resistive component thermal conductivity given by

$$\kappa_{RTA}(Q,\Omega) = \frac{1}{A\delta}\sum_{q,b}\hbar\omega_{q,b}v^2_{q,b}\frac{\tau^C_{q,b}}{1 + j\Omega\tau^C_{q,b} + jQ\Lambda_{q,b}}\frac{\partial N^0_{q,b}}{\partial T} \tag{5}$$

where A and δ are the area of the unit cell and thickness of the graphene monolayer. This κ_{RTA} is the component of thermal conductivity originating from the relaxation time approximation (RTA), where all the scattering mechanisms including normal scattering are treated as resistive. Hence, we refer to κ_{RTA} as the resistive or RTA thermal conductivity. The frequency dependence and non-locality enter the κ_{RTA} through the term $1 + j\Omega\tau^C_{q,b} + jQ\Lambda_{q,b}$ in the denominator, which acts

as a suppression function: when frequency exceeds the scattering rate $\Omega > 1/\tau_{q,b}^{C}$ of a phonon mode or the wavelength is smaller than its MFP $Q^{-1} < \Lambda_{q,b}$, the contribution of that mode to the conductivity is correspondingly reduced.

In graphene, momentum-conserving normal scattering mechanisms are strong and the RTA solution κ_{RTA} underestimates the total thermal conductivity.[72] Following Allen's improved Callaway (AIC) model,[82] the hydrodynamic effect of normal processes is encapsulated as a correction term $\kappa_{corr} = \frac{\lambda_1 \lambda_2}{\lambda_3}$, where

$$\lambda_1(Q,\Omega) = \frac{1}{A\delta}\sum_{q,b} v_{q,b} q_{\parallel} \frac{\tau_{q,b}^{C}}{1 + j\Omega\tau_{q,b}^{C} + jQ\Lambda_{q,b}} \frac{\partial \widetilde{N}_{q,b}^{0}}{\partial T} \tag{6}$$

$$\lambda_2(Q,\Omega) = \frac{1}{A\delta}\sum_{q,b} v_{q,b} q_{\parallel} \left[\frac{\tau_{q,b}^{C}/\tau_{q,b}^{N}}{1 + j\Omega\tau_{q,b}^{C} + jQ\Lambda_{q,b}}\right] \frac{\partial \widetilde{N}_{q,b}^{0}}{\partial T} \tag{7}$$

$$\lambda_3(Q,\Omega) = \frac{1}{A\delta}\sum_{q,b} \frac{q_{\parallel}^{2}}{\hbar\omega_{q,b}} \left[1 - \frac{\tau_{q,b}^{C}/\tau_{q,b}^{N}}{1 + j\Omega\tau_{q,b}^{C} + jQ\Lambda_{q,b}}\right] \frac{\partial \widetilde{N}_{q,b}^{0}}{\partial T} \tag{8}$$

The effective thermal conductivity κ_{eff} is a sum of the RTA, which treats all scattering mechanisms as resistive, and a correction that accounts for an additional collective contribution from momentum-conserving normal processes, both of which are complex-valued and depend on the frequency and spatial wavenumber of the temperature gradient. Similar to κ_{RTA}, each of the correction terms has an Ω- and Q-dependent suppression function. However, the dependence of κ_{corr} due to the combined three terms $\lambda_1\lambda_2\,/\lambda_3$ is more complex than κ_{RTA}.

III. RESULTS AND DISCUSSION

A. Frequency Dependence

First we focus on the effect of the dynamical temperature gradient on thermal conductivity. We separate the temporal dependence from the spatial dependence by setting $Q = 0$ in Eqs. 5-8. Fig. 1a shows the real part of thermal conductivity vs. frequency of the temperature gradient (Ω) for various ribbon sizes at room (300 K) temperature. For any given ribbon size, thermal conductivity shows two distinct behaviors: the first is a constant thermal conductivity regime at low frequencies of the temperature gradient, where the thermal conductivity is equal to its steady-state value $\kappa_{eff}(\Omega = 0)$ and the second is a high frequency regime, where thermal conductivity

exhibits a decaying frequency-dependent behavior with Ω. The high-frequency regime resembles the response of a typical low-pass filter. The zero-frequency (steady-state) thermal conductivity is highest for the flake of dimensions $100\ \mu m \times 100\ \mu m$ (largest size considered here) and lowest for the narrowest ribbon, whose width equals $1.5\ \mu m$, due to the strong edge-roughness scattering in the narrow ribbon.

The low-pass frequency-dependent behavior can be explained as follows: thermal conductivity is a sum of a broad distribution of modal thermal conductivities. At low frequencies, all the thermally-excited phonon modes have sufficient time to undergo multiple scattering events during one cycle of the temperature gradient. As a result, a local thermal equilibrium is restored to yield a steady-state thermal conductivity. In contrast, when the frequency is increased beyond the cut-off, phonons with relaxation times larger than one period of the temperature gradient do not have sufficient time to scatter and equilibrate. Such phonon modes do not fully contribute to conductivity; instead, their contribution is suppressed by an amount determined by the term $(1+j\Omega\tau^C_{q,b})^{-1}$, leading to an apparent reduction in thermal conductivity at high frequencies. Thus, the frequency of temperature oscillations Ω can be used to control which phonon modes contribute towards thermal conductivity, and to what extent, based on their lifetimes. Frequency-dependent measurements can potentially be used to probe the distribution of phonon lifetimes, analogously to recent advances in MFP spectroscopy.[83–85]

The frequency-dependent dynamical suppression is depicted in Fig. 1b, where the mode-dependent thermal conductivity is plotted against their scattering rates for frequencies Ω equal to 0, 10^9, and $10^{10}\ s^{-1}$, shown by black, red, and blue markers respectively. For Ω equal to $10^9\ s^{-1}$, it can be seen that the phonon modes with scattering rates smaller than Ω do not thermalize and thus contribute less towards thermal conductivity than in steady-state. The contribution of phonon modes with small scattering rates to thermal conductivity is further suppressed when Ω equals $10^{10}\ s^{-1}$, while modal thermal conductivities for phonon modes with scattering rates much larger than the frequency of the temperature gradient remain unaffected. The reduced contribution from the phonon modes with scattering rates smaller than Ω is also demonstrated in the cumulative thermal conductivity vs. scattering rate plot shown in the inset of Fig. 1b.

The frequency-dependent thermal conductivity exhibits a low-pass thermal filter behavior, analogous to the frequency response of electrical conductivity for time-varying electric fields, as described by Drude's model. We normalize the frequency-dependent thermal conductivity for a given ribbon size and temperature by dividing with its corresponding steady-state value

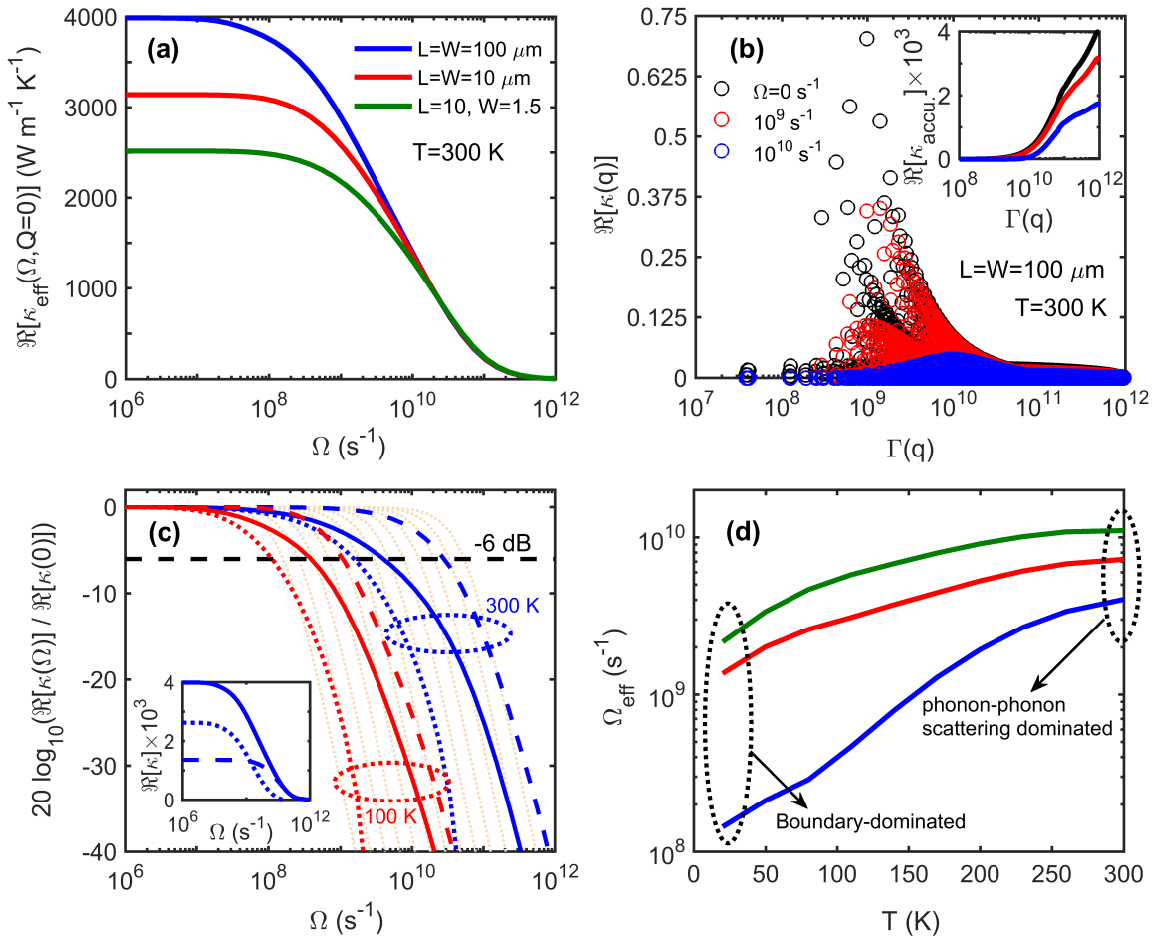

FIG. 1. **(a)** shows the frequency dependence of the real part of thermal conductivity $\Re(\kappa_{eff})$ for several ribbon sizes at 300 K. In **(b)**, the mode-dependent thermal conductivity is plotted against the scattering rate of the corresponding phonon modes at different frequencies of temperature gradient, $\Omega = 0$, 10^9, and 10^{10} s^{-1} shown by black, red and blue markers respectively. The inset in **(b)** shows the accumulative thermal conductivity with modal scattering rates for the same set of frequencies as described by the markers previously. The normalized thermal conductivity $\kappa_{eff}(\Omega)/\kappa_{eff}(\Omega = 0)$ in dB vs. frequency of temperature gradient (Ω) is plotted in **(c)** for 100 and 300 K. The solid, dashed, and dotted lines represent normalized κ_{eff}, κ_{RTA}, and κ_{corr}, respectively. The inset shows the components of thermal conductivity at 300 K. In **(c)**, the size of the ribbon considered is $100\ \mu m \times 100\ \mu m$. The cut-off frequency corresponding to κ_{eff} is plotted against temperature for various ribbon sizes in **(d)**. The rms value of edge roughness is taken to be 2 nm for all the cases.

and then express it in decibels (dB), as one would describe the gain of an electronic filter, $20\log_{10}\left[\kappa_{eff}(\Omega)/\kappa_{eff}(0)\right]$. The solid lines in Fig. 1c show the frequency response of the normalized thermal conductivity in dB at 100 and 300 K temperatures. If all the phonon modes scattered at the same rate, then the two thermal conductivity regimes, constant and frequency-dependent, would be separated by a single corner frequency $\Omega_{corner} = \tau^{-1}$ such that $\kappa(\Omega) = \kappa(0)\,/(1 + j\Omega\tau)$. Multiplying both sides of this expression by ∇T and taking the inverse Fourier transform, as further elaborated in Supplemental Material,[81] produces the Cattaneo-Vernotte (C-V) equation for the heat current $\tau\frac{dJ(x,t)}{dt} + J(x,t) = \kappa(0)\nabla T(x,t)$, which describes wave-like heat transfer with a finite velocity of propagation,[86] x is considered as the direction of transport here. For comparison, the single-τ frequency response is plotted by yellow-dotted lines for different corner frequencies ranging from about 10^8 to 10^{12} Hz.

In contrast, in most solids including graphene, each phonon mode scatters at a vastly different rate. Owing to this broad spectrum of scattering rates, the transition of κ_{eff} from constant at low frequencies to decaying at high frequencies is broad and smooth. In Fig. 1c, the thermal conductivity at both temperatures shows a much gradual decay than the yellow-dotted lines. As there is no single corner frequency to demarcate the transition between the constant thermal conductivity regime at low frequencies and decaying thermal conductivity at high frequencies, we define a cut-off frequency Ω_{eff} where the real part of the thermal conductivity decays to -6 dB or half of its steady-state value, shown by the black-dashed horizontal line in Fig. 1c. The inset in Fig. 1c shows the frequency response of the RTA (κ_{RTA}), correction (κ_{corr}), and effective (κ_{eff}) thermal conductivity at room temperature (RT, 300 K) by the dashed, dotted, and solid lines respectively for a graphene ribbon of size $100\ \mu m \times 100\ \mu m$. κ_{eff} is much greater than κ_{RTA} indicating hydrodynamic transport, where it is no longer sufficient to describe thermal conductivity with the RTA term alone. We normalize the resistive, normal, and effective thermal conductivities by their steady-state values in Fig. 1c and observe different cut-off frequencies for each of the κ_{RTA}, κ_{corr}, and κ_{eff}. In suspended graphene ribbons, where a major fraction of the scattering events are momentum-conserving normal scattering, the heat flux is dissipated at a much slower rate than the purely resistive case and the relaxation time is larger than the one obtained under the RTA, leading to $\Omega_{RTA} > \Omega_{eff} > \Omega_{corr}$.

As Ω_{eff} is closely associated with the scattering rates, it can be tuned by both temperature and size of the ribbon. In Fig. 1d, the cut-off frequencies for various ribbon sizes have been plotted against temperature. For a given ribbon size, owing to the increase in phonon-phonon scattering

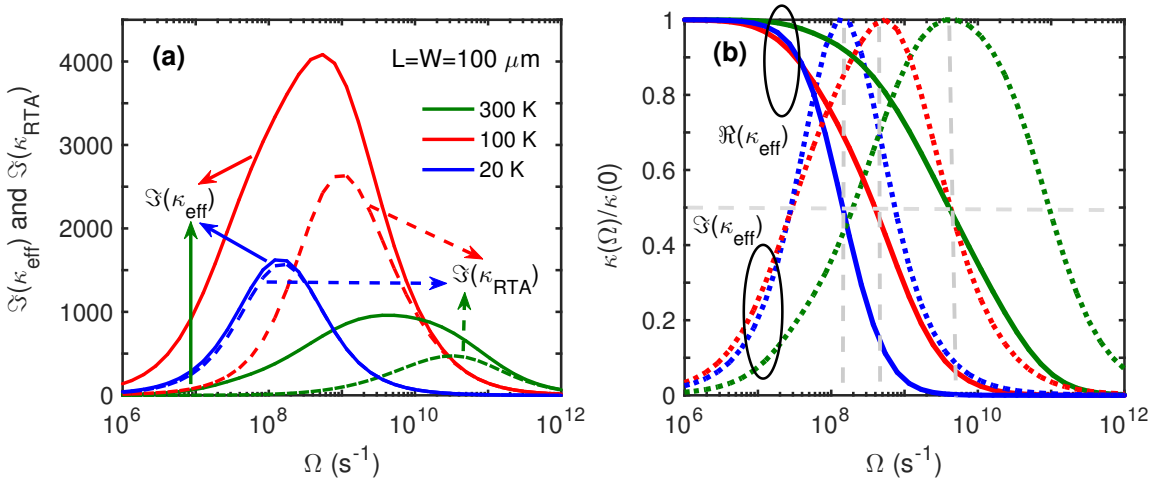

FIG. 2. **(a)** Imaginary part of thermal conductivity vs. frequency of the temperature gradient for $L = W = 100\ \mu m$ at 20, 100, and 300 K. The frequency response of the $\Im(\kappa_{RTA})$ is shown by the dashed lines for different temperatures. **(b)** shows the normalized real as well as the imaginary part of thermal conductivity for the same set of temperatures and ribbon size. The solid lines represent the normalized $\Re(\kappa_{eff})$ and the dotted-lines their imaginary counterparts $\Im(\kappa_{eff})$.

with temperature Ω_{eff} shows an increasing trend. At a given temperature, Ω_{eff} decreases with increasing ribbon size, which we attribute to the decrease in the boundary scattering with increasing ribbon size. At temperatures around 300 K, the size dependence of Ω_{eff} becomes weak because phonon-phonon scattering dominates over the boundary scattering. The cut-off frequencies in graphene ribbons are found to range from 100 MHz to 2 GHz at 20 K, and 3-10 GHz at room temperature, depending on ribbon width. We contrast these frequencies to the analogous behavior of high-frequency electrical conductivity of graphene, which was found to follow a Drude model[87] with a decay at frequencies exceeding 4-6 THz, depending on substrate and carrier concentration.[88] Hence, there is a wide swath of frequencies between $\sim$3 GHz and $\sim$4 THz where thermal conductivity is strongly suppressed while electrical conductivity is at its DC value, offering a potential avenue for dynamic enhancement of the thermoelectric figure-of-merit $ZT(\Omega) \propto \sigma(\Omega)/\kappa(\Omega)$.[89]

The dynamical thermal conductivity can be split into real and imaginary parts, where $\Re(\kappa_{eff})$ is related to heat flux dissipation via scattering while the imaginary part of the thermal conductivity is related to the storage of thermal energy in the ballistic phonon modes. The imaginary component turns the heat diffusion equation (HDE) $\rho C_V dT/dt = \kappa d^2T/dx^2$ into a dampened wave equation;

in fact, a purely imaginary conductivity turns the HDE into a wave equation, analogous to the Schrödinger equation, admitting solutions of the form $T(x,t) \propto \exp[j(Qx - \Omega t)]$ that satisfy $j\Omega\rho C_V T = -\kappa(\Omega, Q)Q^2 T$ (ρ and C are density and specific heat capacity). Furthermore, the relative sizes of the real and imaginary components dictate the phase of the heat flux relative to the temperature gradient that drives it, with the imaginary component representing phase lag. This lagging behavior can be traced back to the C-V equation, which is to first order equivalent to $J(x, t+\tau) = -\kappa(0)\nabla T(x,t)$,[90] with τ being the flux-gradient phase lag. The frequency response of the imaginary part of thermal conductivity $\Im(\kappa_{eff})$, shown by the solid curves in Fig. 2a for 100 $\mu m \times 100$ μm at different temperatures. $\Im(\kappa_{eff})$ shows an increasing trend beyond the frequency where the real part of thermal conductivity starts to fall off. Then $\Im(\kappa_{eff})$ peaks before decaying to zero at high frequencies. The height of the peak depends on temperature in the same way as the steady-state thermal conductivity.

The dashed and solid lines in Fig. 2a represent the imaginary parts of the RTA component $\Im(\kappa_{RTA})$ and total thermal conductivity $\Im(\kappa_{eff})$; the imaginary part of correction κ_{corr} is omitted for clarity. At both 100 and 300 K, $\Im(\kappa_{RTA})$ peaks at a higher frequency than the corresponding $\Im(\kappa_{eff})$ due to the presence of strong normal scattering, associated with hydrodynamic thermal transport, indicating that the RTA component has a smaller phase delay. There is a window of frequencies between the two peaks where κ_{corr} is complex, thus lagging in phase, while κ_{RTA} is real and in-phase with the gradient. In Fig. 2b, we observe that the imaginary part of thermal conductivity peaks at the same frequency Ω_{eff} where the real part of thermal conductivity decays to half of its steady-state value. Thus, the peak of the imaginary part can also be used to determine the cut-off frequency, at which the phase angle between flux and gradient is 45° for a first-order and 90° for a second-order frequency slope. In the frequency range between Ω_{eff} and Ω_{RTA}, the κ_{corr} will be complex while κ_{RTA} is still real-valued, indicating a phase difference between these two components of the heat flux.

B. Spatial Dependence

Now we turn to the spatial dependence of thermal conductivity. To isolate it from the temporal response of thermal conductivity, we set Ω=0 in Eqs. (5-8). The real part of thermal conductivity is plotted in Fig. 3 against the wavelength (Q^{-1}) of the temperature gradient for ribbon dimensions ranging from 1.5 to 100 μm at 300 K. The wavelength of temperature gradient Q^{-1} is the relevant

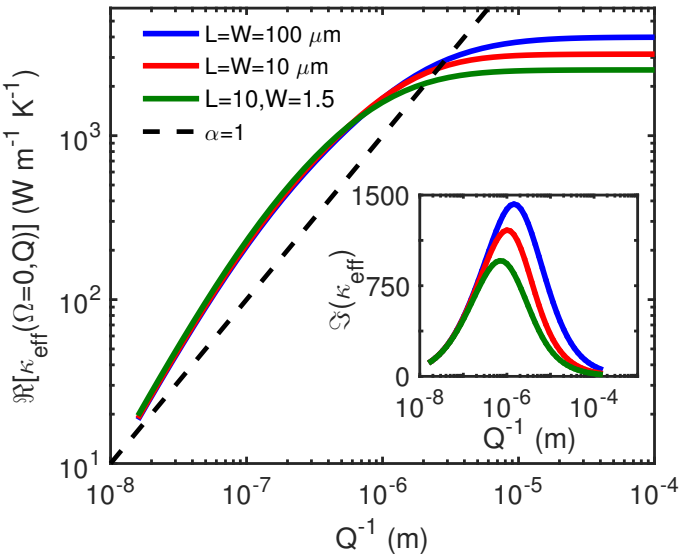

FIG. 3. Real part of the thermal conductivity vs. wavelength of temperature gradient (Q^{-1}) for several ribbon sizes at 300 K, showing super-linear scaling in the narrow ($Kn < 1$) regime. Dashed line indicates a linear ($\propto Q^{-\alpha}$ with $\alpha = 1$) trend for comparison. The inset shows the corresponding wavelength dependence of the imaginary part of thermal conductivity.

lengths scale; when it is larger than the phonon MFP (Λ), all the phonons undergo multiple scattering events within a single temperature node, leading to thermalization. On the other hand, when the wavelength is comparable to the phonon MFP, a fraction of the phonons having $\Lambda > Q^{-1}$ travel ballistically and do not scatter on the length scale over which the temperature is varying. The modal dependence is captured by the suppression $1/(1 + jQ\Lambda_{q,b})$ in Eqs. (5-8), where the dimensionless term $Kn = Q\Lambda_{q,b}$ plays the role of an effective modal Knudsen number. This also leads to an apparent reduction of thermal conductivity for $Kn > 1$, as observed previously in thermal grating experiments,[41] and in narrow ribbons of width $W < \Lambda_{avg}$; Λ_{avg} being the phonon MFP averaged over all phonon modes and across all branches. When the ribbon edges are rough, heat flux decays at the edges due to diffuse scattering and components of the flux having whose wavelength exceeds the width, or $QW < 1$, are suppressed so the wavelength dependence informs us about size scaling. Fig. 3 shows that in narrow ribbons, thermal conductivity scales as $\kappa \propto Q^{-\alpha}$ with a slope $\alpha > 1$, indicating super-linear scaling. In contrast to the ballistic-to-diffusive transition[91] where size scaling is sub-linear, the hydrodynamic correction κ_{corr} has a stronger size

dependence as all three terms Eqs. (6-8) explicitly depend on Q. The imaginary component of thermal conductivity is shown in the inset, displaying a peak around the same wavelength where the real part reduces to one-half of its $Q = 0$ value. At the peak, $Kn = 1$ and the wavelength equals the average phonon MFP $Q^{-1} = \Lambda_{avg} \approx 1\ \mu$m.[79]

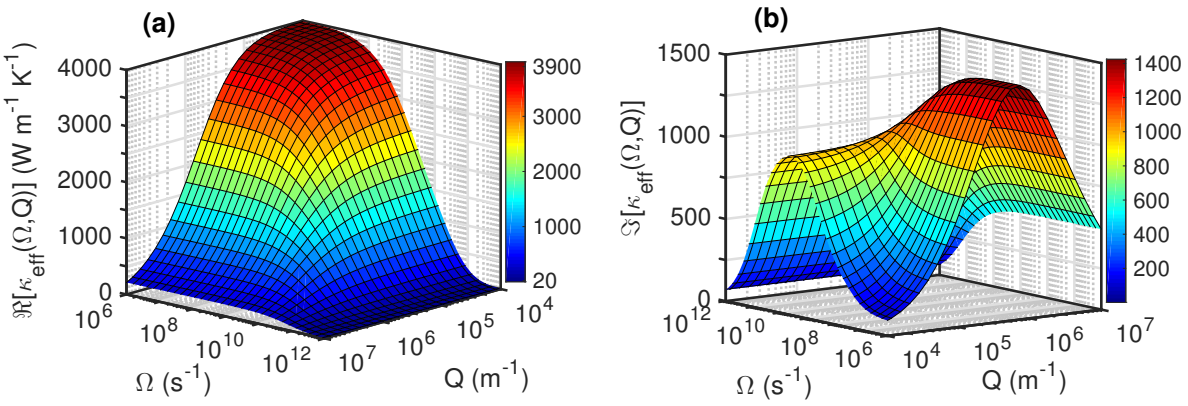

FIG. 4. Surface plots of the frequency and spatial dependence of real part in **(a)** and imaginary part in **(b)** of thermal conductivity in a graphene ribbon of size L=W=100 μm and at 300 K.

The complete temporal and spatial dependence of the thermal conductivity at RT are shown in Fig. 4a and 4b, respectively. At small wavenumbers (Q) and frequencies (Ω) of temperature gradient, the real part of thermal conductivity goes to its highest value $\Re[\kappa_{eff}(\Omega = 0, Q = 0)]$ for a given temperature and ribbon size. The $\Re[\kappa_{eff}(\Omega, Q)]$ decays to zero when either Ω exceeds the average scattering rate or the wavelength $Q^{-1} \ll \Lambda_{avg}$, the average phonon MFP. For any intermediate values, $\Re[\kappa_{eff}(\Omega, Q)]$ decays from $\Re[\kappa_{eff}(0, 0)]$ to zero with increasing Q and Ω. The imaginary part of thermal conductivity against frequency and wavenumber of the temperature gradient is plotted in Fig. 4b. For small wavenumbers, $Q^{-1} \ll \Lambda$, $\Im[\kappa_{eff}(\Omega, Q)]$ shows a resonant behavior: it is equal to zero at low as well as high frequencies with a peak at the cut-off frequency (also shown in Fig. 2). $\Im[\kappa_{eff}(\Omega, Q)]$ vs. Q shows a similar trend for small frequencies below the scattering rate, also shown in the inset of Fig. 3. However, for intermediate values of Ω and Q, the imaginary part of thermal conductivity exhibits a very interesting behavior: for $Q \gg 10^5 m^{-1}$, it is constant and decays to zero at high frequencies of temperature gradient. On the other hand, for Ω close to the cut-off, $\Im[\kappa_{eff}]$ starts constant, then reaches a broad peak where $Q^{-1} = \Lambda_{avg}$ (Kn =1) before decaying to zero at very high wavenumbers $Q \gg 10^7 m^{-1}$, implying larger phase

shift for spatially localized or peaked heat pulses whose wavelength is around the phonon MFP $\approx$1 μm.

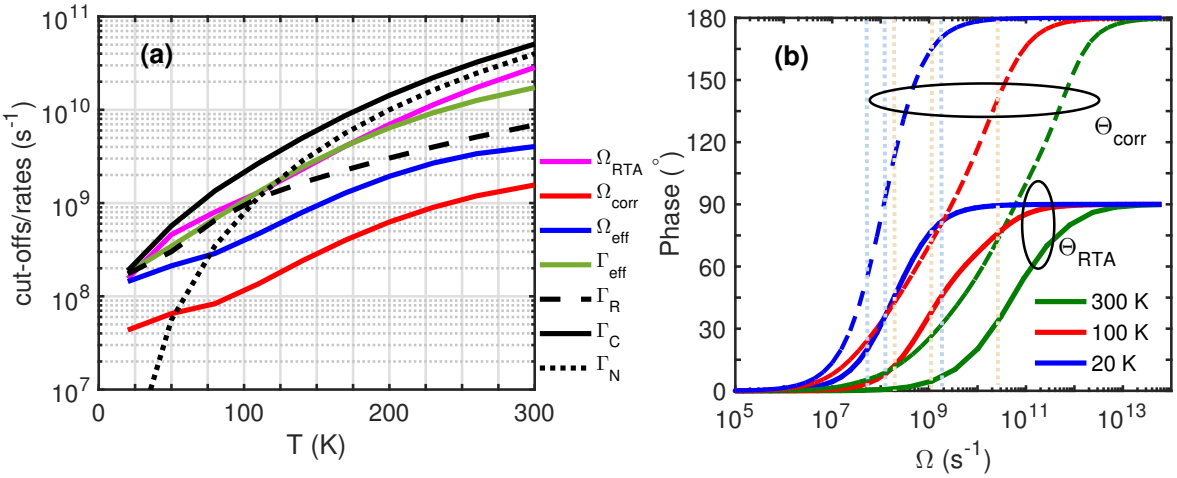

FIG. 5. **(a)** shows the combined, normal, and resistive scattering rates along with the cut-off frequencies for a ribbon size of $L = W = 100\ \mu m$ as a function of temperature ranging from 20 to 300 K. **(b)** variation in phase of κ_{RTA} (solid) and κ_{corr} (dashed lines) vs. frequency at T=20 (blue), 200 (red), and 300 K (green), showing first and second-order behavior, respectively, along with a constant lag in the second sound frequency window $\Gamma_R < \Omega < \Gamma_N$, marked by vertical dashed lines in colors matching the corresponding temperatures.

C. Conductivity in the Second Sound Regime

The propagation of a heat pulse in the form of a temperature wave is referred to as second sound. For a material to host such a wave-like thermal transport, the primary condition is that it should exhibit hydrodynamic transport,which occurs when there is significantly more momentum-conserving normal scattering than momentum-destroying resistive scattering mechanisms. Then there exists a "window" of frequencies $\Gamma_R < \Omega < \Gamma_N$[61] where second sound can be observed. This makes suspended graphene a promising candidate to host second sound even at room temperature.[56] Second sound has also been characterized by a two-fluid flow where superfluid (in this case hydrodynamic, represented by κ_{corr}) and non-superfuid (here resistive, κ_{RTA}) components are out of phase.[92] This is in contrast to purely ballistic transport where all the components of the heat flux are in phase. We compare the cut-off frequencies to the scattering rates, which are all

plotted in Fig. 5a as a function of temperature for a large ($L = W$ =100 μm) graphene flake. Ω_{RTA} corresponds to the cut-off frequency of κ_{RTA} from to the combined scattering rate $\Gamma_C = \Gamma_R + \Gamma_N$, while Ω_{corr} and Ω_{eff} represent cut-off frequencies corresponding to κ_{corr} and κ_{eff}, respectively. The frequency window $\Gamma_R < \Omega < \Gamma_N$ coincides with the regime where the dissipative and hydrodynamic components of thermal conductivity, κ_{RTA} and κ_{corr}, are out of phase by a constant shift, shown in Fig. 5b. Ultimately, we find that the hydrodynamic transport should be treated as two fluxes, each with its own lag arising out of the corresponding cut-off frequencies Ω_{RTA} and Ω_{corr}.

IV. CONCLUSION

We have studied the dynamical response of thermal conductivity to time- and spatially-varying temperature gradients at several temperatures and ribbon sizes. We derived a compact and computationally efficient model for dynamical thermal conductivity by Fourier-transforming the pBTE, while including first-principles phonon dispersion and differentiating between resistive and normal scattering mechanisms. We found that the frequency-dependent thermal conductivity in suspended graphene resembles a low-pass thermal filter, whose cut-off frequency is related to the scattering rate and can be tuned over a wide range from a few MHz to several GHz by size and temperature. At low temperatures when the phonon-phonon scattering is weak, the cut-off frequency rises inversely to ribbon width. The RTA contribution always has a higher cut-off, related to the total scattering rate, than the hydrodynamic correction. Both are complex-valued in the transition region, indicating a phase lag. The dynamical response of thermal conductivity can be used as a platform for phonon lifetime spectroscopy in frequency-dependent measurements. The dual cut-offs and phase lags of the two components of heat flux can be employed to study the hydrodynamic phenomenon of second sound.

ACKNOWLEDGMENTS

This work has been supported by the National Science Foundation Emerging Frontiers in Research and Innovation (EFRI) 2-DARE grant 1542864.

APPENDIX

To obtain an expression for $\widetilde{\Phi}_{q,b}(Q,\Omega)$, we first Fourier-transform the time-dependent pBTE (Eq. 2), akin to the work by Ezzahri and Joulain,[46] and write the pBTE in Fourier domain as

$$\begin{aligned} &j\Omega\widetilde{\Phi}_{q,b} + j\Omega\widetilde{N}^0_{q,b} + j\vec{Q}\cdot\vec{v}_{q,b}\widetilde{\Phi}_{q,b} + \vec{v}_{q,b}\cdot\widetilde{\nabla}T(Q,\Omega)\frac{\partial\widetilde{N}^0_{q,b}}{\partial T} \\ &= -\frac{\widetilde{N}_{q,b}-\widetilde{N}^0_{q,b}}{\tau^R_{q,b}} - \frac{\widetilde{N}_{q,b}-\widetilde{N}^*_{q,b}}{\tau^N_{q,b}}, \end{aligned} \tag{A.9}$$

where the right-hand side is the collision term from Eq. (3). The flowing equilibrium $\widetilde{N}^*_{q,b}$ is expanded around $\vec{\lambda}=0$ in a Taylor series,[46,82] keeping terms up to first order in $\vec{\lambda}$

$$\widetilde{N}^*_{q,b} \approx \widetilde{N}^*_{q,b}(\vec{\lambda}=0) + \vec{\lambda}\cdot\left(\frac{\partial\widetilde{N}^*_{q,b}}{\partial\vec{\lambda}}\right)_{\vec{\lambda}=0} = \widetilde{N}^0_{q,b} - \frac{k_B T^2}{\hbar\omega_{q,b}}\frac{\partial\widetilde{N}^0_{q,b}}{\partial T}(\vec{\lambda}\cdot\vec{q}). \tag{A.10}$$

On replacing $\widetilde{N}^*_{q,b}$ on the right side of Eq. (A.9) with the expression in Eq. (A.10), and $\widetilde{N}_{q,b}-\widetilde{N}^0_{q,b}$ with $\widetilde{\Phi}_{q,b}$, we write Eq. (A.9) as

$$\begin{aligned} &j\Omega\widetilde{\Phi}_{q,b} + j\Omega\widetilde{N}^0_{q,b} + j\vec{Q}\cdot\vec{v}_{q,b}\widetilde{\Phi}_{q,b} + \vec{v}_{q,b}\cdot\widetilde{\nabla}T(Q,\Omega)\frac{\partial\widetilde{N}^0_{q,b}}{\partial T} \\ &= -\frac{\widetilde{\Phi}_{q,b}}{\tau^C_{q,b}} - \frac{1}{\tau^N_{q,b}}\left[\frac{k_B T^2}{\hbar\omega_{q,b}}\frac{\partial\widetilde{N}^0_{q,b}}{\partial T}\vec{\lambda}\cdot\vec{q}\right], \end{aligned} \tag{A.11}$$

where $1/\tau^R_{q,b} + 1/\tau^N_{q,b}$ is the combined quasi-particle relaxation rate $1/\tau^C_{q,b}$.[82] By rearranging the terms, $\widetilde{\Phi}_{q,b}$ can be written as

$$\begin{aligned} \widetilde{\Phi}_{q,b}(Q,\Omega) = &-\frac{\tau^C_{q,b}}{1+j\Omega\tau^C_{q,b}+jQ\Lambda_{q,b}}\vec{v}_{q,b}\cdot\widetilde{\nabla}T(Q,\Omega)\frac{\partial\widetilde{N}^0_{q,b}}{\partial T} \\ &-\frac{\tau^C_{q,b}/\tau^N_{q,b}}{1+j\Omega\tau^C_{q,b}+jQ\Lambda_{q,b}}\frac{k_B T^2}{\hbar\omega_{q,b}}\frac{\partial\widetilde{N}^0_{q,b}}{\partial T}(\vec{\lambda}\cdot\vec{q}) - j\Omega\widetilde{N}^0_{q,b}\tau^C_{q,b}, \end{aligned} \tag{A.12}$$

where $\Lambda_{q,b} = v_{q,b}\tau^C_{q,b}$ is the modal phonon MFP and Q is the component of the wavevector of the temperature gradient $\vec{Q}$, both along the direction of transport.

To obtain an expression for the displacement of the drifted distribution $\vec{\lambda}$ we follow Allen's improved Callaway (AIC) model,[82] according to which the total crystal momentum should be the same for both the actual distribution $\widetilde{N}_{q,b}$ and the flowing equilibrium $\widetilde{N}^*_{q,b}$. This means

$$\sum_{q,b}\vec{q}(\widetilde{N}_{q,b}-\widetilde{N}^*_{q,b}) = 0 = \sum_{q,b}\vec{q}(\widetilde{\Phi}_{q,b}+\widetilde{N}^0_{q,b}-\widetilde{N}^*_{q,b}). \tag{A.13}$$

Using the Taylor series expansion for $\widetilde{N}^*_{q,b}$ obtained in Eq. (A.10), we write $\widetilde{N}^0_{q,b} - \widetilde{N}^*_{q,b}$ on the right hand side of Eq. (A.13) as

$$\widetilde{N}^0_{q,b} - \widetilde{N}^*_{q,b} = \frac{k_B T^2}{\hbar\omega_{q,b}} \frac{\partial \widetilde{N}^0_{q,b}}{\partial T} \vec{\lambda} \cdot \vec{q}. \tag{A.14}$$

Taking $\vec{\lambda}$ to be in the direction of the applied temperature gradient, $\vec{\lambda} \cdot \vec{q}$ can be simplified to $\lambda q_{\parallel}$, where $q_{\parallel}$ is the phonon wavevector in the transport direction. Then, combining Eqs. (A.12) and (A.14), $\widetilde{\Phi}_{q,b}$ and $\widetilde{N}^0_{q,b} - \widetilde{N}^*_{q,b}$ can be replaced in Eq. (A.13) to solve for the displacement

$$\widetilde{\lambda}(Q,\Omega) = \frac{\displaystyle\sum_{q,b} q_{\parallel} \left(\frac{\tau^C_{q,b}}{1 + j\Omega\tau^C_{q,b} + jQ\Lambda_{q,b}} v_{q,b} \frac{\partial \widetilde{N}^0_{q,b}}{\partial T} \right) \widetilde{\nabla} T(Q,\Omega) + j\Omega \sum_{q,b} \vec{q} \widetilde{N}^0_{q,b} \tau^C_{q,b}}{\displaystyle\sum_{q,b} q_{\parallel}^2 \frac{\partial \widetilde{N}^0_{q,b}}{\partial T} \frac{k_B T^2}{\hbar\omega_{q,b}} \left(1 - \frac{\tau^C_{q,b}/\tau^N_{q,b}}{1 + j\Omega\tau^C_{q,b} + jQ\Lambda_{q,b}} \right)}. \tag{A.15}$$

The term $\displaystyle\sum_{q,b} q \widetilde{N}^0_{q,b} \tau^C_{q,b}$ in the numerator of Eq. (A.15) is equal to zero because both the equilibrium distribution and the scattering rates are even functions while the wavevector $\vec{q}$ is odd; consequently, the displacement $\widetilde{\lambda}(Q,\Omega) \propto \widetilde{\nabla} T(Q,\Omega)$. We also find $\widetilde{\lambda}$ to be dependent on both wavenumber Q and frequency Ω, unlike earlier derivations that assumed it to be constant.[46] The deviation $\widetilde{\Phi}_{q,b}$ can now be expressed by substituting $\widetilde{\lambda}(Q,\Omega)$ in Eq. A.12. Now $\widetilde{\Phi}_{q,b}(Q,\Omega)$ is replaced in Eq. 4 to obtain thermal conductivity as a function of wavenumber and frequency.

---

* zlatana@engin.umass.edu

[1] D. A. Broido, M. Malorny, G. Birner, N. Mingo, and D. A. Stewart. Intrinsic lattice thermal conductivity of semiconductors from first principles. *Appl. Phys. Lett.*, 91(23):231922, 2007.

[2] A. Ward and D. A. Broido. Intrinsic phonon relaxation times from first-principles studies of the thermal conductivities of Si and Ge. *Phys. Rev. B*, 81(8):085205, 2010.

[3] A. Jain and A. J. H. McGaughey. Thermal transport by phonons and electrons in aluminum, silver, and gold from first principles. *Phys. Rev. B*, 93:081206, 2016.

[4] B. D. Kong, S. Paul, M. B. Nardelli, and K. W. Kim. First-principles analysis of lattice thermal conductivity in monolayer and bilayer graphene. *Phys. Rev. B*, 80(3):033406, 2009.

[5] A. A. Balandin. Thermal properties of graphene and nanostructured carbon materials. *Nat Mater*, 10(8):569–581, 2011.

[6] L. Lindsay, W. Li, J. Carrete, N. Mingo, D. A. Broido, and T. L. Reinecke. Phonon thermal transport in strained and unstrained graphene from first principles. *Phys. Rev. B*, 89:155426, 2014.

[7] X. Xu, L. F. C. Pereira, Y. Wang, J. Wu, K. Zhang, X. Zhao, S. Bae, C. T. Bui, R. Xie, J. T. L. Thong, B. H. Hong, K. P. Loh, D. Donadio, B. Li, and B. Özyilmaz. Length-dependent thermal conductivity in suspended single-layer graphene. *Nat. Commun.*, 5:3689, 2014.

[8] A. K. Majee and Z. Aksamija. Length divergence of the lattice thermal conductivity in suspended graphene nanoribbons. *Phys. Rev. B*, 93:235423, 2016.

[9] L. Lindsay, D. A. Broido, and T. L. Reinecke. First-principles determination of ultrahigh thermal conductivity of boron arsenide: A competitor for diamond? *Phys. Rev. Lett.*, 111:025901, 2013.

[10] C. Chiritescu, D. G. Cahill, N. Nguyen, D. Johnson, A. Bodapati, P. Keblinski, and P. Zschack. Ultralow thermal conductivity in disordered, layered WSe_2 crystals. *Science*, 315(5810):351–353, 2007.

[11] E. T. Swartz and R. O. Pohl. Thermal boundary resistance. *Rev. Mod. Phys.*, 61(3):605–668, 1989.

[12] S. P. Hepplestone and G. P. Srivastava. Theory of interface scattering of phonons in superlattices. *Phys. Rev. B*, 82:144303, 2010.

[13] P. E. Hopkins, J. C. Duda, and P. M. Norris. Anharmonic phonon interactions at interfaces and contributions to thermal boundary conductance. *J. Heat Transf.*, 133:062401, 2011.

[14] Z. Aksamija and I. Knezevic. Anisotropy and boundary scattering in the lattice thermal conductivity of silicon nanomembranes. *Phys. Rev. B*, 82:045319, 2010.

[15] H. Dong, B. Wen, and R. Melnik. Relative importance of grain boundaries and size effects in thermal conductivity of nanocrystalline materials. *Sci. Rep.*, 4:7037, 2014.

[16] P. Yasaei, A. Fathizadeh, R. Hantehzadeh, A. K. Majee, A. El-Ghandour, D. Estrada, C. Foster, Z. Aksamija, F. Khalili-Araghi, and A. Salehi-Khojin. Bimodal phonon scattering in graphene grain boundaries. *Nano Lett.*, 15:4532–4540, 2015.

[17] A. I. Hochbaum, R. Chen, R. D. Delgado, W. Liang, E. C. Garnett, M. Najarian, A. Majumdar, and P. Yang. Enhanced thermoelectric performance of rough silicon nanowires. *Nature*, 451:163–167, 2008.

[18] M. Upadhyaya and Z. Aksamija. Non-diffusive lattice thermal transport in Si-Ge alloy nanowires. *Phys. Rev. B*, accepted, 2016.

[19] P. Martin, Z. Aksamija, E. Pop, and U. Ravaioli. Impact of phonon-surface roughness scattering on thermal conductivity of thin Si nanowires. *Phys. Rev. Lett.*, 102(12):125503, 2009.

[20] E. S. Landry and A. J. H. McGaughey. Effect of film thickness on the thermal resistance of confined semiconductor thin films. *J. Appl. Phys.*, 107(1):013521, 2010.

[21] C. Jeong, S. Datta, and M. Lundstrom. Thermal conductivity of bulk and thin-film silicon: A Landauer approach. *J. Appl. Phys.*, 111(9):093708, 2012.

[22] G. Chen. Thermal conductivity and ballistic-phonon transport in the cross-plane direction of superlattices. *Phys. Rev. B*, 57(23):14958–14973, 1998.

[23] D. A. Broido and T. L. Reinecke. Lattice thermal conductivity of superlattice structures. *Phys. Rev. B*, 70(8):081310, 2004.

[24] Z. Aksamija and I. Knezevic. Thermal conductivity of $si_{1-x}ge_x/si_{1-y}ge_y$ superlattices: Competition between interfacial and internal scattering. *Phys. Rev. B*, 88:155318, 2013.

[25] X. Wang, Y. Hong, P. K L Chan, and J. Zhang. Phonon thermal transport in silicene-germanene superlattice: a molecular dynamics study. *Nanotechnology*, 28:255403, 2017.

[26] R. Yang and Gang Chen. Thermal conductivity modeling of periodic two-dimensional nanocomposites. *Phys. Rev. B*, 69(19):195316, 2004.

[27] Z. Aksamija. Lattice thermal transport in si-based nanocomposites for thermoelectric applications. *J. Elec. Mater.*, 44(6):1644–1650, 2015.

[28] J.-K. Yu, S. Mitrovic, D. Tham, J. Varghese, and J. R. Heath. Reduction of thermal conductivity in phononic nanomesh structures. *Nat Nano*, 5:718–721, 2010.

[29] G. Pernot, M. Stoffel, I. Savic, F. Pezzoli, P. Chen, G. Savelli, A. Jacquot, J. Schumann, U. Denker, I. Mnch, Ch. Deneke, O. G. Schmidt, J. M. Rampnoux, S. Wang, M. Plissonnier, A. Rastelli, S. Dilhaire, and N. Mingo. Precise control of thermal conductivity at the nanoscale through individual phonon-scattering barriers. *Nat Mater*, 9:491–495, 2010.

[30] D. Abarbanel and J. Maassen. Modeling quasi-ballistic transient thermal transport with spatially sinusoidal heating: A mckelvey-shockley flux approach. *J. Appl. Phys.*, 121(20):204305, 2017.

[31] C. W. Chang, D. Okawa, H. Garcia, A. Majumdar, and A. Zettl. Breakdown of fourier's law in nanotube thermal conductors. *Phys. Rev. Lett.*, 101:075903, 2008.

[32] M. E. Siemens, Q. Li, R. Yang, K. A. Nelson, E. H. Anderson, M. M. Murnane, and H. C. Kapteyn. Quasi-ballistic thermal transport from nanoscale interfaces observed using ultrafast coherent soft x-ray beams. *Nat Mater*, 9:26–30, 2010.

[33] G. Chen. Nonlocal and nonequilibrium heat conduction in the vicinity of nanoparticles. *Journal of Heat Transfer*, 118:539–545, 1996.

[34] N. Mingo and D. A. Broido. Carbon nanotube ballistic thermal conductance and its limits. *Phys. Rev. Lett.*, 95(9):096105, 2005.

[35] M. N. Luckyanova, J. Garg, K. Esfarjani, A. Jandl, M. T. Bulsara, A. J. Schmidt, A. J. Minnich, S. Chen, M. S. Dresselhaus, Z. Ren, E. A. Fitzgerald, and G. Chen. Coherent phonon heat conduction in superlattices. *Science*, 338(6109):936–939, 2012.

[36] G. D. Mahan and F. Claro. Nonlocal theory of thermal conductivity. *Phys. Rev. B*, 38:1963–1969, 1988.

[37] G. Chen. Ballistic-diffusive heat-conduction equations. *Phys. Rev. Lett.*, 86:2297–2300, 2001.

[38] A. J. Minnich, J. A. Johnson, A. J. Schmidt, K. Esfarjani, M. S. Dresselhaus, K. A. Nelson, and G. Chen. Thermal conductivity spectroscopy technique to measure phonon mean free paths. *Phys. Rev. Lett.*, 107(9):095901, 2011.

[39] J. P. Freedman, J. H. Leach, E. A. Preble, Z. Sitar, R. F. Davis, and J. A. Malen. Universal phonon mean free path spectra in crystalline semiconductors at high temperature. *Sci. Rep.*, 3:2963, 2013.

[40] J. A. Johnson, A. A. Maznev, J. Cuffe, J. K. Eliason, A. J. Minnich, T. Kehoe, C. M. S. Torres, G. Chen, and K. A. Nelson. Direct measurement of room-temperature nondiffusive thermal transport over micron distances in a silicon membrane. *Phys. Rev. Lett.*, 110:025901, 2013.

[41] L. Zeng, K. C. Collins, Y. Hu, Maria N. Luckyanova, A. A. Maznev, S. Huberman, V. Chiloyan, J. Zhou, X. Huang, K. A. Nelson, and G. Chen. Measuring phonon mean free path distributions by probing quasiballistic phonon transport in grating nanostructures. *Sci. Rep.*, 5:17131, 2015.

[42] P. B. Allen. Size effects in thermal conduction by phonons. *Phys. Rev. B*, 90:054301, Aug 2014.

[43] A J Minnich. Advances in the measurement and computation of thermal phonon transport properties. *J. Phys.: Condens. Matter*, 27(5):053202, 2015.

[44] S. G. Volz. Thermal insulating behavior in crystals at high frequencies. *Phys. Rev. Lett.*, 87:074301, 2001.

[45] F. X. Alvarez and D. Jou. Memory and nonlocal effects in heat transport: From diffusive to ballistic regimes. *Appl. Phys. Lett.*, 90(8):083109, 2007.

[46] Y. Ezzahri and K. Joulain. Dynamical thermal conductivity of bulk semiconductor crystals. *J. Appl. Phys.*, 112(8):083515, 2012.

[47] Y. Ezzahri and A. Shakouri. Ballistic and diffusive transport of energy and heat in metals. *Phys. Rev. B*, 79:184303, 2009.

[48] Y. Ezzahri, K. Joulain, and A. Shakouri. Transient energy and heat transport in metals: Effect of the discrete character of the lattice. *J. Heat Transfer*, 133:072401–072401–14, 2011.

[49] P. Bhalla, P. Kumar, N. Das, and N. Singh. Theory of the dynamical thermal conductivity of metals. *Phys. Rev. B*, 94:115114, 2016.

[50] H. Kaburaki, J. Li, S. Yip, and H. Kimizuka. Dynamical thermal conductivity of argon crystal. *J. Appl. Phys.*, 102:043514, 2007.

[51] A. Sellitto, F. X. Alvarez, and D. Jou. Phonon-wall interactions and frequency-dependent thermal conductivity in nanowires. *J. Appl. Phys.*, 109(6):064317, 2011.

[52] F. Yang and C. Dames. Heating-frequency-dependent thermal conductivity: An analytical solution from diffusive to ballistic regime and its relevance to phonon scattering measurements. *Phys. Rev. B*, 91:165311, 2015.

[53] J. Callaway. Model for lattice thermal conductivity at low temperatures. *Phys. Rev.*, 113:1046–1051, 1959.

[54] L. Chaput. Direct solution to the linearized phonon boltzmann equation. *Phys. Rev. Lett.*, 110:265506, 2013.

[55] S. Ghosh, I. Calizo, D. Teweldebrhan, E. P. Pokatilov, D. L. Nika, A. A. Balandin, W. Bao, F. Miao, and C. N. Lau. Extremely high thermal conductivity of graphene: Prospects for thermal management applications in nanoelectronic circuits. *Appl. Phys. Lett.*, 92(15):151911, 2008.

[56] S. Lee, David B., K. Esfarjani, and G. Chen. Hydrodynamic phonon transport in suspended graphene. *Nat. Commun.*, 6:6290, 2015.

[57] Y. Guo and M. Wang. Phonon hydrodynamics and its applications in nanoscale heat transport. *Physics Reports*, 595:1 – 44, 2015. Phonon hydrodynamics and its applications in nanoscale heat transport.

[58] J. Zhang, X. Huang, Y. Yue, J. Wang, and X. Wang. Dynamic response of graphene to thermal impulse. *Phys. Rev. B*, 84:235416, 2011.

[59] A. Cepellotti, G. Fugallo, L. Paulatto, M. Lazzeri, F. Mauri, and N. Marzari. Phonon hydrodynamics in two-dimensional materials. *Nat. Commun.*, 6:6400, 2015.

[60] M. Chester. Second sound in solids. *Phys. Rev.*, 131:2013–2015, 1963.

[61] R. A. Guyer and J. A. Krumhansl. Dispersion relation for second sound in solids. *Phys. Rev.*, 133:A1411–A1417, 1964.

[62] R. A. Guyer and J. A. Krumhansl. Solution of the linearized phonon boltzmann equation. 148:766–778, 1966.

[63] A. Cepellotti and N. Marzari. Transport waves as crystal excitations. *Phys. Rev. Materials*, 1:045406, 2017.

[64] C. T. Lane, H. A. Fairbank, and W. M. Fairbank. Second sound in liquid helium ii. *Phys. Rev.*, 71:600–605, 1947.

[65] T. F. McNelly, S. J. Rogers, D. J. Channin, R. J. Rollefson, W. M. Goubau, G. E. Schmidt, J. A. Krumhansl, and R. O. Pohl. Heat pulses in naf: Onset of second sound. *Phys. Rev. Lett.*, 24:100–102, 1970.

[66] H. E. Jackson, C. T. Walker, and T. F. McNelly. Second sound in naf. *Phys. Rev. Lett.*, 25:26–28, 1970.

[67] V. Narayanamurti and R. C. Dynes. Observation of second sound in bismuth. *Phys. Rev. Lett.*, 28:1461–1465, 1972.

[68] M. Markov, J. Sjakste, G. Barbarino, G. Fugallo, L. Paulatto, M. Lazzeri, F. Mauri, and N. Vast. Hydrodynamic heat transport regime in bismuth: A theoretical viewpoint. *Phys. Rev. Lett.*, 120:075901, 2018.

[69] A. Koreeda, R. Takano, and S. Saikan. Second sound in $\mathrm{srtio_3}$. *Phys. Rev. Lett.*, 99:265502, 2007.

[70] Y. K. Koh, D. G. Cahill, and B. Sun. Nonlocal theory for heat transport at high frequencies. *Phys. Rev. B*, 90:205412, 2014.

[71] M. Omini and A. Sparavigna. An iterative approach to the phonon boltzmann equation in the theory of thermal conductivity. *Physica B: Condensed Matter*, 212(2):101 – 112, 1995.

[72] L. Lindsay, D. A. Broido, and N. Mingo. Flexural phonons and thermal transport in graphene. *Phys. Rev. B*, 82(11):115427, 2010.

[73] A. Chernatynskiy and S. R. Phillpot. Evaluation of computational techniques for solving the boltzmann transport equation for lattice thermal conductivity calculations. *Phys. Rev. B*, 82:134301, 2010.

[74] J. Ma, W. Li, and X. Luo. Examining the callaway model for lattice thermal conductivity. *Phys. Rev. B*, 90:035203, 2014.

[75] Y. Guo and M. Wang. Heat transport in two-dimensional materials by directly solving the phonon boltzmann equation under callaway's dual relaxation model. *Phys. Rev. B*, 96:134312, 2017.

[76] Z. Ding, J. Zhou, B. Song, V. Chiloyan, M. Li, T.-H. Liu, and G. Chen. Phonon hydrodynamic heat conduction and knudsen minimum in graphite. *Nano Letters*, 18(1):638–649, 2018. PMID: 29236507.

[77] P. Giannozzi, S. Baroni, N. Bonini, M. Calandra, R. Car, C. Cavazzoni, D. Ceresoli, G. L Chiarotti, M. Cococcioni, I. Dabo, A. D. Corso, S. de Gironcoli, S. Fabris, G. Fratesi, R. Gebauer, U. Gerstmann, C. Gougoussis, A. Kokalj, M. Lazzeri, L. Martin-Samos, N. Marzari, F. Mauri, R. Mazzarello, S. Paolini, A. Pasquarello, L. Paulatto, C. Sbraccia, S. Scandolo, G. Sclauzero, A. P. Seitsonen, A. Smogunov, P. Umari, and R. M Wentzcovitch. Quantum espresso: a modular and open-source software project for quantum simulations of materials. *J. Phys. Condens. Matter*, 21(39):395502, 2009.

[78] D. T. Morelli, J. P. Heremans, and G. A. Slack. Estimation of the isotope effect on the lattice thermal

conductivity of group IV and group III-V semiconductors. *Phys. Rev. B*, 66(19):195304, 2002.

[79] Z. Aksamija and I. Knezevic. Lattice thermal conductivity of graphene nanoribbons: anisotropy and edge roughness scattering. *Appl. Phys. Lett.*, 98:141919, 2011.

[80] Z. Aksamija and I. Knezevic. Thermal transport in graphene nanoribbons supported on sio_2. *Phys. Rev. B*, 86:165426, 2012.

[81] See Supplemental Material at [URL to be inserted here] for further details on the expressions of scattering rates and their temperature and size dependence, frequency and spatial dependence of magnitude and phase of real part of thermal conductivity, and thermodynamic equations for dynamical thermal conductivity.

[82] P. B. Allen. Improved callaway model for lattice thermal conductivity. *Phys. Rev. B*, 88:144302, Oct 2013.

[83] K. T. Regner, D. P. Sellan, Z. Su, C. H. Amon, A. J.H. McGaughey, and J. A. Malen. Broadband phonon mean free path contributions to thermal conductivity measured using frequency domain thermoreflectance. *Nat Commun*, 4:1640, 2013.

[84] J. Cuffe, J. K. Eliason, A. A. Maznev, K. C. Collins, J. A. Johnson, A. Shchepetov, M. Prunnila, J. Ahopelto, C. M. S. Torres, G. Chen, and K. A. Nelson. Reconstructing phonon mean-free-path contributions to thermal conductivity using nanoscale membranes. *Phys. Rev. B*, 91:245423, 2015.

[85] H. Zhang, X. Chen, Y.-D. Jho, and A. J. Minnich. Temperature-dependent mean free path spectra of thermal phonons along the c-axis of graphite. *Nano Lett.*, 16:1643–1649, 2016.

[86] D. D. Joseph and L. Preziosi. Heat waves. *Rev. Mod. Phys.*, 61:41–73, 1989.

[87] N. Sule, S. C. Hagness, and I. Knezevic. Clustered impurities and carrier transport in supported graphene. *Phys. Rev. B*, 89:165402, 2014.

[88] L. Ren, Q. Zhang, J. Yao, Z. Sun, R. Kaneko, Z. Yan, S. Nanot, Z. Jin, I. Kawayama, M. Tonouchi, J. M. Tour, and J. Kono. Terahertz and infrared spectroscopy of gated large-area graphene. *Nano Lett.*, 12(7):3711–3715, 2012.

[89] Y. Ezzahri and K. Joulain. Dynamical thermoelectric coefficients of bulk semiconductor crystals: Towards high thermoelectric efficiency at high frequencies. *J. Appl. Phys.*, 115(22):223703, 2014.

[90] D. Y. Tzou. A unified field approach for heat conduction from macro- to micro-scales. *J. Heat Transf.*, 117(1):8–16, 1995.

[91] M.-H. Bae, Z. Li, Z. Aksamija, P. N. Martin, F. Xiong, Z.-Y. Ong, I. Knezevic, and E. Pop. Ballistic to diffusive crossover of heat flow in graphene ribbons. *Nat. Commun.*, 4:1734, 2013.

[92] L. A. Sidorenkov, M. K. Tey, R. Grimm, Y.-H. Hou, L. Pitaevskii, and S. Stringari. Second sound and the superfluid fraction in a fermi gas with resonant interactions. *Nature*, 498:78, 2013.